Available online at www.sciencedirect.com
SCIENCE DIRECT®
Journal of Computational Physics 207 (2005) 240–260
JOURNAL OF COMPUTATIONAL PHYSICS
www.elsevier.com/locate/jcp

# Preconditioning method for condensate fluid and solid coupling problems in general curvilinear coordinates

Satoru Yamamoto

*Department of Computer and Mathematical Sciences, Tohoku University, Aramaki Aza Aoba01, Sendai 980-8579, Japan*

Received 19 April 2004; received in revised form 19 January 2005; accepted 19 January 2005
Available online 22 February 2005

**Abstract**

A preconditioned flux-vector splitting (PFVS) scheme in general curvilinear coordinates which can be applied to condensate fluid and solid coupling problems is presented and some typical calculated results are shown to prove the availability of the present method. This method is based on the preconditioning method applied to compressible Navier–Stokes (NS) equations with additional equations and source terms for condensate flows. Since the present PFVS terms composed of the convective and pressure terms of the NS equations are completely reduced to only the pressure terms when the velocities are set to zero, the present scheme can further applied to the calculation not only for a dynamic field but also for a static field including a transitional field from the dynamic region to the static region. In this paper, as a first stage of the present study, coupling problems between a condensate flow in a flow field and heat conduction in a solid structure are simultaneously calculated by using the present method. As numerical examples, transonic and low speed flows around the NACA0012 airfoil, nonequilibrium condensate flows in a nozzle, and natural convection with condensation around a pipe at 1g and zero gravity are simulated with heat conduction in the solid structure.


*Keywords:* Preconditioning method; Condensate flow; Heat conduction; Coupling problem

## 1. Introduction

Compressible flow solvers have a certain problem, the so-called stiff problem, when a flow at very low Mach number is calculated. No convergence of solution may be obtained. Turkel [1], Choi and Merkle [2] and Weiss and Smith [3] have proposed the preconditioning method to overcome the stiffness in the compressible flow solvers. A numerical speed of sound has been additionally introduced with the

*E-mail address:* yamamoto@caero.mech.tohoku.ac.jp.

0021-9991/$ - see front matter © 2005 Elsevier Inc. All rights reserved.
doi:10.1016/j.jcp.2005.01.013

**Nomenclature**

| | |
|---|---|
| $c$ | speed of sound |
| $e$ | total internal energy per unit volume |
| $g_{ij}$ | metrics $\nabla\xi_i \cdot \nabla\xi_j$ |
| $I$ | unit matrix |
| $I_c$ | nucleation rate |
| $J$ | Jacobian for transformation |
| $n$ | number density of nucleus (or particulates) |
| $p$ | static pressure |
| $Re$ | Reynolds number |
| $r$ | averaged radius of water droplets |
| $T$ | static temperature |
| $t$ | physical time |
| $x_i$ | Cartesian coordinates |
| $U_i$ | contravariant velocity components |
| $\boldsymbol{u}$ | physical velocity vectors |
| $u_i$ | physical velocity components |
| $\rho$ | total density |
| $\rho_{\mathrm{v}}$ | density of water vapor |
| $\rho_\ell$ | density of water liquid |
| $\beta$ | condensate mass fraction |
| $\Gamma$ | preconditioning matrix |
| $\Gamma_{\mathrm{c}}$ | condensate mass generation rate |
| $\gamma$ | specific heat |
| $\Delta t$ | time interval |
| $\kappa$ | heat conductivity coefficient |
| $\mu$ | molecular viscosity coefficient |
| $\xi_i$ | general curvilinear coordinates |
| $\tau_{ij}$ | viscosity stress tensor |

*Symbols*

| | |
|---|---|
| a | dry air |
| v | water vapor |
| g | mixed gas |
| m | multi phase |
| s | saturated condition |
| $n$ | time step |

pseudo-compressibility into compressible flow solvers as a preconditioning procedure. As a result, fundamental equations are transformed to incompressible Navier–Stokes equations with the pseudo-compressibility and the thermal equation only at very low Mach number. We can also find other approaches related to the preconditioning method. Dailey and Pletcher [4] presented a preconditioning approach applied to time-accurate calculations using both explicit and implicit schemes. Edwards and Liou [5] developed a preconditioning method based on the advective upwind splitting method (AUSM). The recent progress of the preconditioning method was summarised by Turkel [6].

The most critical case in the preconditioning may be that the Mach number is zero. Then, all terms multiplied by the velocities should be disappeared from the Navier–Stokes (NS) equations and only the pressure terms and the equation of heat conduction remains theoretically. It means that the numerical fluxes for the convective and pressure term derived according to the preconditioning approach should be proven to reduce to only the pressure terms without any numerical dissipation. If one gets the property allowing the zero-velocity field in compressible flow solvers, the flow solvers may extend to some critical flow problems including static fields or solid structures. Of course, the solid structure can be solved by existing typical commercial codes. However, most of the existing codes can not solve transitional problems from fluids to solids, the so-called phase-change problems such as the icing of moist air around a body and the crystal growth at micro-gravity.

Recently, our group developed a preconditioned flux-vector splitting (PFVS) scheme in general curvilinear coordinates [7] based on the preconditioning techniques [2,3]. This scheme has been further applied to the Roe scheme [8] and the LU-SGS scheme [9]. The present PFVS form can be completely reduced to only the pressure terms when the velocities set to zero in it.

At first in this paper, the PFVS scheme is extended to the fundamental equations for condensate flow problems. Then, the fundamental equations for transonic condensate flows with homogeneous [10] and heterogeneous nucleation [11] are transformed to preconditioned equations. Especially, the fundamental formulas which are necessary to derive the PFVS scheme in general curvilinear coordinates are described in detail.

The second issue of this paper is that the present method is applied to coupling problems between a condensate flow in a flow field and heat conduction in a solid structure. In condensation problems, heat due to the condensation, the so-called latent heat, is released at the surrounding region of the condensation. The local heating affects the performance of aircrafts and steam turbines. Also this heating may cause the erosion in the pipe where a wet-steam flows. Therefore, the prediction of the heating rate not only in condensate flows but also in solid structures contacting with the flow is quite important. In this paper as numerical examples, condensate fluid-solid coupling problems, such as transonic and low speed flows around the NACA0012 airfoil, homogeneous condensate flows in a nozzle, and natural convection with condensation around a pipe are calculated with heat conduction in the solid structure.

One of the final targets of this study is to calculate any fluid-solid coupling problem with phase transition between two phases such as crystal-growth (CG) problems. In this paper, the CG problem is not studied, but as a preliminary study, a natural convection with condensation around a pipe with heat conduction in the solid structure was calculated by assuming zero gravity. Then, the calculated zero-velocity field could make condensation around the pipe associate with only the cooling from the pipe surface.

## 2. Fundamental equations

The fundamental equations for two-dimensional compressible viscous flows of moist air are composed of conservation laws of the total density, the momentums, the total energy, the density of water vapor, the density of water liquid, and the number density of nucleus [10]. When water droplets are sufficiently small, a homogeneous flow without velocity slips among air, water vapor and water liquid can be assumed. Then, the system of two-dimensional equations is written in a vector form by

$$\partial \boldsymbol{q}/\partial t + L(\boldsymbol{q}) = \frac{\partial \boldsymbol{q}}{\partial t} + \frac{\partial \boldsymbol{f}_i}{\partial x_i} + \frac{\partial \boldsymbol{f}_{vi}}{\partial x_i} + \boldsymbol{s} = 0 \quad (i = 1, 2), \tag{1}$$

where

$$\boldsymbol{q} = \begin{bmatrix} \rho \\ \rho u_1 \\ \rho u_2 \\ e \\ \rho_v \\ \rho\beta \\ \rho n \end{bmatrix}, \quad \boldsymbol{f}_i = \begin{bmatrix} \rho u_i \\ \rho u_1 u_i + \delta_{i1} p \\ \rho u_2 u_i + \delta_{i2} p \\ (e+p)u_i \\ \rho_v u_i \\ \rho\beta u_i \\ \rho n u_i \end{bmatrix}$$

$$\boldsymbol{f}_{vi} = -\begin{bmatrix} 0 \\ \tau_{i1} \\ \tau_{i2} \\ \tau_{ik}u_k + \kappa \partial T/\partial x_i \\ 0 \\ 0 \\ 0 \end{bmatrix}, \quad \boldsymbol{s} = -\begin{bmatrix} 0 \\ 0 \\ 0 \\ 0 \\ -\Gamma_c \\ \Gamma_c \\ \rho I_c \end{bmatrix},$$

where $\boldsymbol{q}$, $\boldsymbol{f}_i$, $\boldsymbol{f}_{vi}$, and $\boldsymbol{s}$ are the vector of unknown variables, the inviscid flux, the viscous flux and the source term. In this study, Eq. (1) is transformed to the system equation in general curvilinear coordinates ($\xi_1$ $\xi_2$). A set of the equations is written by

$$\frac{\partial Q}{\partial t} + \frac{\partial F_i}{\partial \xi_i} + \frac{\partial F_{vi}}{\partial \xi_i} + S = 0 \quad (i = 1, 2), \tag{2}$$

where

$$Q = J\boldsymbol{q}, \quad F_i = J(\partial \xi_i/\partial x_j)\boldsymbol{f}_j, \quad F_{vi} = J(\partial \xi_i/\partial x_j)\boldsymbol{f}_{vj}, \quad S = J\boldsymbol{s}$$

$$J = \partial(x_1 x_2)/\partial(\xi_1 \xi_2).$$

The equation of state and the speed of sound have been introduced by Ishizaka, Ikohagi and Daiguji [12] assuming that the mass fraction of water liquid $\beta$ is sufficiently small ($\beta < 0.1$). These equations are given by

$$p = \rho R T (1 - \beta), \tag{3}$$

$$c = \left[\frac{C_{pm}}{C_{pm} - (1-\beta)R}\frac{p}{\rho}\right]^{1/2}, \tag{4}$$

where

$$R = \left(\frac{\rho_a R_u}{\rho_g M_a} + \frac{\rho_v R_u}{\rho_g M_v}\right),$$

where $\rho_a$ and $\rho_g$ are the densities of dry air and mixed gas. $M_a$ and $M_v$ are the molecular weights of dry air and water vapor. $R_u$ is the universal gas constant. $C_{pm}$ is defined by the linear combination of the specific heat at constant pressure between gas phase and liquid phase using $\beta$. The viscous stress tensor $\tau_{ij}$ is given by

$$\tau_{ij} = (\mu + \mu_t)\left[\left(\frac{\partial u_i}{\partial x_j} + \frac{\partial u_j}{\partial x_i}\right) - \frac{2}{3}\delta_{ij}\frac{\partial u_k}{\partial x_k}\right] \quad (i, j = 1, 2). \tag{5}$$

The molecular viscosity $\mu$ is also derived from the linear combination between that of gas phase and that of liquid phase using $\beta$. $\mu_t$ is the eddy viscosity. The Baldwin–Lomax turbulence model [13] is used to evaluate $\mu_t$ in this study.

## 3. Condensation model

In wind tunnel experiments, onset of condensation may be dominated by homogeneous nucleation [10]. On the other hand, natural condensation is observed in atmospheric flight conditions. In this condensation, the onset may be governed by heterogeneous nucleation and almost equilibrium condensation [11].

The mass generation rate $\Gamma_c$ of water droplets are composed of the nucleation rate and the growth rate. The growth rate originally derived by Hall [14] has been simplified by Ishizaka, Ikohagi and Daiguji [12]. In this study, this simplified model is also employed. Then, the mass generation rate $\Gamma_c$ is defined by

$$\Gamma_c = \frac{4}{3}\pi\rho_\ell I r_*^3 + 4\pi\rho_\ell n r^2 \frac{\mathrm{d}r}{\mathrm{d}t}, \tag{6}$$

where $I_c$ is the homogeneous nucleation rate defined by Frenkel [15] as

$$I_c = q_c\left(\frac{2\sigma}{\pi m^3}\right)^{1/2}\frac{\rho_v^2}{\rho_\ell}\exp\left(-\frac{4\pi r_*^2\sigma}{3kT}\right), \tag{7}$$

where $q_c$, $\sigma$, $m$ and $k$ are the condensation coefficient, the surface tension of a water droplet, the molecular weight of water, and the Boltzmann constant. $r_*$ is the critical radius of nucleus defined by

$$r_* = \frac{2\sigma}{\rho_\ell RT\ln(s)},$$

where $s = p/p_s(T)$ is the supercritical ratio of water vapor and $p_s(T)$ is the saturation pressure of water vapor. The time derivative of radius of a water droplet $\mathrm{d}r/\mathrm{d}t$ in the growth rate is assumed to satisfy the Hertz–Knudsen's law in which the droplet radius is much smaller than the mean free-path of a water molecule. A simplified model for $\mathrm{d}r/\mathrm{d}t$ presented by Schnerr and Dohrmann [16] is used. The saturation pressure for a water droplet of radius $r$ is given by the Kelvin–Helmholtz equation. On the other hand, heterogeneous nucleation in this study is modeled by assuming a constant radius and a constant number of particulates in atmospheric flow conditions as same as the model already used by Yamamoto [11].

## 4. Preconditioning procedure

### 4.1. Fundamental equations

The preconditioning method developed by Weiss and Smith [3] is applied to Eq. (2). The unknown variables in the unknown vector $\hat{Q}$ for the preconditioned equations is defined as $\hat{Q} = J[p\ u_1\ u_2\ T\ \rho_v/\rho\ \beta\ n]^T$, then the set of preconditioned equations is derived from Eq. (2) by using a preconditioning matrix $\Gamma$ as

$$\Gamma\partial\hat{Q}/\partial t + L(\hat{Q}) = \Gamma\frac{\partial\hat{Q}}{\partial t} + \frac{\partial F_i}{\partial\xi_i} + \frac{\partial F_{vi}}{\partial\xi_i} + S = 0 \quad (i = 1, 2), \tag{8}$$

where

$$\Gamma = \begin{bmatrix} \theta & 0 & 0 & \rho_T & 0 & 0 & 0 \\ \theta u_1 & \rho & 0 & \rho_T u_1 & 0 & 0 & 0 \\ \theta u_2 & 0 & \rho & \rho_T u_2 & 0 & 0 & 0 \\ \theta H - 1 & \rho u_1 & \rho u_2 & \rho_T H + \rho C_p & 0 & 0 & 0 \\ \theta \rho_v/\rho & 0 & 0 & \rho_T \rho_v/\rho & \rho & 0 & 0 \\ \theta\beta & 0 & 0 & \rho_T \beta & 0 & \rho & 0 \\ \theta n & 0 & 0 & \rho_T n & 0 & 0 & \rho \end{bmatrix}.$$

$H = (e + p)/\rho$. $\rho_T = \partial\rho/\partial T$. $\theta$ is the preconditioning parameter and this is defined by $\theta = (1/U_r^2 - \rho_T/\rho C_p)$. The switching parameter $U_r$ was defined by Weiss and Smith [3]. In this paper,

$$U_r = \begin{cases} \epsilon c & (u < \epsilon c), \\ u & (\epsilon c < u < c), \\ c & (c < u), \end{cases}$$

where $u = \sqrt{u_i u_i}$. $\epsilon$ is a very small number as same as that by Weiss and Smith [3]. No additional modifications were taken into consideration for $U_r$ in this study.

Eq. (2) can be solved by a finite-difference method based on an approximate Riemann solver. We have developed a high-resolution finite-difference method to solve Eq. (2) for simulating unsteady transonic viscous flows. In this method, the fourth-order compact MUSCL TVD (Compact MUSCL) scheme [17], Roe's approximate Riemann solver [8] and the LU-SGS scheme [9] have been employed. These schemes are extended to schemes for the present preconditioning method as follows.

### 4.2. Preconditioned flux-vector splitting

The numerical flux $(F_i)_{\ell+1/2}$ for $F_i$ in Eq. (8) defined at the interface between the control volume $\ell$ and $\ell + 1$ in each coordinate $i$ ($i = 1, 2$) can be written by a flux-vector splitting form as

$$(F_i)_{\ell+1/2} = (F_i^+)_{\ell+1/2} + (F_i^-)_{\ell+1/2} = (\hat{A}_i^+)_{\ell+1/2}\hat{Q}^{\mathrm{L}}_{\ell+1/2} + (\hat{A}_i^-)_{\ell+1/2}\hat{Q}^{\mathrm{R}}_{\ell+1/2}. \tag{9}$$

The superscripts $\pm$ indicate the sign of characteristic speeds. $F_i^{\pm}$ are the numerical flux-vectors composed of only positive or negative characteristic speeds. $\hat{A}_i^{\pm}$ are the preconditioned Jacobian matrices composed of only positive or negative characteristic speeds. $\hat{Q}^{\mathrm{L}}$ and $\hat{Q}^{\mathrm{R}}$ are the unknown vectors extrapolated by the compact MUSCL [17] from left and right directions. The preconditioned flux-vector splitting form for $(\hat{A}_i^{\pm})_{\ell+1/2}\hat{Q}^{\mathrm{M}}_{\ell+1/2}$ derived in this study is given by

$$(\hat{A}_i^{\pm})_{\ell+1/2}\hat{Q}^{\mathrm{M}} = (\Gamma L_i^{-1} \Lambda_i^{\pm} L_i)_{\ell+1/2}\hat{Q}^{\mathrm{M}} = \hat{\lambda}_{i1}^{\pm}\Gamma\hat{Q}^{\mathrm{M}} + \frac{\hat{\lambda}_{ia}^{\pm}}{\hat{c}_i\sqrt{g_{ii}}}\hat{Q}_{ia} + \frac{\hat{\lambda}_{ib}^{\pm}}{\hat{c}_i^2}\hat{Q}_{ib}. \tag{10}$$

The superscript M is replaced by L or R. $L_i$ and $\Lambda_i$ are the matrices composed of preconditioned eigenvectors and preconditioned characteristic speeds (eigenvalues). $\hat{\lambda}_{ia}^{\pm}$ and $\hat{\lambda}_{ib}^{\pm}$ are defined by

$$\hat{\lambda}_{ia}^{\pm} = (\hat{\lambda}_{i3}^{\pm} - \hat{\lambda}_{i4}^{\pm})/2,$$
$$\hat{\lambda}_{ib}^{\pm} = (\ell_i^- \hat{\lambda}_{i3}^{\pm} - \ell_i^+ \hat{\lambda}_{i4}^{\pm})/(\ell_i^- - \ell_i^+) - \hat{\lambda}_{i1}^{\pm},$$

where $\hat{\lambda}_{ij}^{\pm}$ ($j = 1, 3, 4$) and $\ell_i^{\pm}$ are calculated by

$$\hat{\lambda}_{ij}^{\pm} = (\hat{\lambda}_{ij} \pm |\, \hat{\lambda}_{ij}\,|)/2,$$
$$\ell_i^{\pm} = \rho U_r^2/(U_i(1-\alpha)/2 \pm \hat{c}_i\sqrt{g_{ii}}),$$

$\hat{\lambda}_{ij}(j = 1, 3, 4)$ are the preconditioned characteristic speeds derived as

$$\hat{\lambda}_{i1} = U_i,$$
$$\hat{\lambda}_{i3} = (1+\alpha)U_i/2 + \hat{c}_i\sqrt{g_{ii}},$$
$$\hat{\lambda}_{i4} = (1+\alpha)U_i/2 - \hat{c}_i\sqrt{g_{ii}},$$

where $\hat{c}_i$ is the numerical speed of sound. It is defined by

$$\hat{c}_i = \sqrt{U_i^2(1-\alpha)^2/g_{ii} + 4U_r^2}\Big/2.$$

$\alpha = U_r^2(\rho_p + \rho_T/\rho C_p)$, where $\rho_p = \partial\rho/\partial p$. If $U_r$ equals the physical speed of sound, $\alpha$ is reduced to unit and characteristic speeds and physical speed of sound for compressible flows are recovered in Eq. (8). $\hat{Q}_{ia}$ and $\hat{Q}_{ib}$ are the subvectors defined by

$$\hat{Q}_{ia} = \hat{q}_1^{\mathrm{M}} Q_{ic} + \rho\hat{U}_i Q_d,$$
$$\hat{Q}_{ib} = (\rho\hat{U}_i\hat{c}_i^2/g_{ii})Q_{ic} + (\hat{q}_1^{\mathrm{M}}\hat{c}_i^2/U_r^2)Q_d,$$

where $\hat{q}_j^{\mathrm{M}}$ and $\hat{U}_i[= (\partial\xi_i/\partial x_j)\hat{q}_{j+1}^{\mathrm{M}}(j = 1, 2)]$ are the $j$th element of $\hat{Q}$ and the contravariant velocities extrapolated by the compact MUSCL [17] in which M = L or R, respectively. $Q_{ic}$ and $Q_d$ are the subvectors given by

$$Q_{ic} = [\,0 \quad \partial\xi_i/\partial x_1 \quad \partial\xi_i/\partial x_2 \quad U_i \quad 0 \quad 0 \quad 0\,]^{\mathrm{T}},$$
$$Q_d = [\,1 \quad u_1 \quad u_2 \quad H \quad \rho_v/\rho \quad \beta \quad n\,]^{\mathrm{T}}.$$

Now, the physical velocities $(u_1, u_2) = (0, 0)$ are substituted into Eq. (10) to get the numerical flux in a zero-velocity field. Then, the first term and the third term of the right-hand side (RHS) in Eq. (10) are reduced to zero because of $\hat{\lambda}_{i1}^{\pm} = \hat{\lambda}_{ib}^{\pm} = 0$. While, only the pressure term is remained in the second term of the RHS in Eq. (10). Finally, the numerical flux derived is written by

$$(\hat{A}_i^{\pm})_{\ell+1/2}\hat{Q}^{\mathrm{M}} = [\,0 \quad (\partial\xi_i/\partial x_1)_{\ell+1/2}\cdot p^{\mathrm{M}} \quad (\partial\xi_i/\partial x_2)_{\ell+1/2}\cdot p^{\mathrm{M}} \quad 0 \quad 0 \quad 0 \quad 0\,]^{\mathrm{T}},$$

where $p^{\mathrm{M}}$ is the MUSCL extrapolated pressure. None of any numerical dissipations are included in this equation at the level of the flux-vector as compared with the existing numerical flux such as that derived by Weiss and Smith [3] where a pressure dissipation is added in it. Therefore, the pressure field in a static field can be accurately calculated. If no pressure difference is specified in the static field, the preconditioned Eq. (8) is completely reduced to only the equation of heat conduction.

### 4.3. Preconditioned flux-difference splitting

The preconditioned flux-vector splitting form is modified to the preconditioned flux-difference splitting form. The Roe scheme is extended to the preconditioned Roe scheme by using this form. The numerical flux $(F_i)_{\ell+1/2}$ for $F_i$ in Eq. (8) defined at the interface between the control volume $\ell$ and $\ell+1$ in each coordinate $i(i = 1, 2)$ can be alternatively written by the flux-difference splitting form according to the previous our study [18] as

$$(F_i)_{\ell+1/2} = \frac{1}{2}\left[F_i(\hat{Q}^{\mathrm{L}}_{\ell+1/2}) + F_i(\hat{Q}^{\mathrm{R}}_{\ell+1/2}) - |\,(\hat{A}_i)_{\ell+1/2}\,|\,(\hat{Q}^{\mathrm{R}}_{\ell+1/2} - \hat{Q}^{\mathrm{L}}_{\ell+1/2})\right], \tag{11}$$

where $|(\hat{A}_i)_{\ell+1/2}|\hat{Q}^{\mathrm{M}}(\mathrm{M} = \mathrm{L}\text{ or }\mathrm{R})$ is defined by

$$|(\hat{A}_i)_{\ell+1/2}|\hat{Q}^{\mathrm{M}} = |\hat{\lambda}_{i1}|\Gamma\hat{Q}^{\mathrm{M}} + \frac{|\hat{\lambda}_{ia}|}{\hat{c}_i\sqrt{g_{ii}}}\hat{Q}_{ia} + \frac{|\hat{\lambda}_{ib}|}{\hat{c}_i^2}\hat{Q}_{ib}. \tag{12}$$

### 4.4. Preconditioned LU-SGS scheme

The flux-vector splitting form Eq. (10) can be also applied to the LU-SGS scheme. The preconditioned LU-SGS scheme is derived as

$$\Gamma D\Delta\hat{Q}^{*} = \mathrm{RHS} + \Delta t G^{+}(\Delta\hat{Q}^{*}), \tag{13}$$

$$\Delta\hat{Q} = \Delta\hat{Q}^{*} - \Gamma^{-1}D^{-1}\Delta t G^{-}(\Delta\hat{Q}), \tag{14}$$

where $D$ is the diagonal matrix approximated by the spectral radius of the preconditioned Jacobian matrices and RHS is the vector of explicit time-marching residues for Eq. (8) defined by

$$D = I + \Delta t[r(\hat{A}_i) + r_{\mathrm{v}}(\partial F_{vi}/\partial\hat{Q})],$$
$$r(\hat{A}) = \alpha_{\mathrm{c}}\max[\lambda(\hat{A})],$$
$$\mathrm{RHS} = -\Delta t L(\hat{Q}^{n}),$$

where $\alpha_c$ is an empirical parameter ($\alpha_c \geqslant 1.0$). $\lambda(\hat{A})$ means the eigenvalues of $\hat{A}$. $r_v(\partial F_{vi}/\partial\hat{Q})$ are exactly the spectral radius of the Jacobian matrix $\partial F_{vi}/\partial\hat{Q}$. In this study, these values were approximately set up to $\alpha_v(\mu + \mu_t + \kappa)g_{ii}/(\rho\Delta\xi_i)$, where $\alpha_v$ is an empirical parameter. In this paper, $\alpha_v$ was set up to 2.0 after some trial and error calculations. $G^{\pm}$ are composed of non-diagonal time-derivative fluxes defined by

$$G^{+}(\Delta\hat{Q}^{*}) = (\hat{A}_1^{+}\Delta\hat{Q}^{*})_{i-1,j} + (\hat{A}_2^{+}\Delta\hat{Q}^{*})_{i,j-1},$$
$$G^{-}(\Delta\hat{Q}) = (\hat{A}_1^{-}\Delta\hat{Q})_{i+1,j} + (\hat{A}_2^{-}\Delta\hat{Q})_{i,j+1},$$

where the subscript $(i, j)$ indicates the grid point where the time-derivative flux is defined. These fluxes are calculated by using Eq. (10). Then, $\hat{Q}^{\mathrm{M}}$ in Eq. (10) is replaced by $\Delta\hat{Q}$.

## 5. Results

### 5.1. Transonic and low speed flows around NACA0012 airfoil

As the first numerical examples, the present preconditioning method is applied to simple two-dimensional flow problems without condensation. Ideal-gas flows around the NACA0012 airfoil at very low Mach number are first calculated to check the convergence of solution. The flow conditions are specified: the angle of attack is 0°, the uniform Mach number is 0.01 or 0.1, the Reynolds number is 2*E*3 or 2*E*4. A C-type computational grid which has $221 \times 93$ grid points is used for all cases. Fig. 1 shows the residues of the continuity equation. All four cases in Fig. 1 get a steady state solution within four thousand iterations.

Fig. 2 shows the calculated Mach number contours around the airfoil for the case of the Mach number 0.01 and the Reynolds number 2*E*4. These results indicate that the present method works very well for simulating very-low-speed flows without the stiffness in the solution.

A transonic flow around the NACA0012 airfoil at 2° angle of attack is next calculated and the calculated result is compared with that calculated by the compressible flow solver developed by our group. The flow conditions are specified: the uniform Mach number is 0.75 and the Reynolds number is $1.2 \times 10^6$. The computational grid used has same grid points with the previous case.

Fig. 3 shows the calculated pressure distributions on the airfoil surface. The calculated result using the present preconditioning method is compared with that obtained by the compressible flow solver and the experiments. Both results are obtained after 20,000 time steps. Then, at least three orders of the continuity residual decrease in both cases. The present result is in good agreement with the experiments, and the

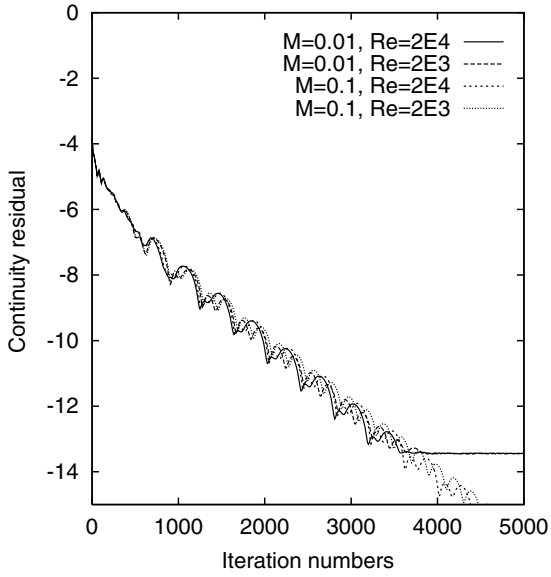


Fig. 1. Continuity residuals.

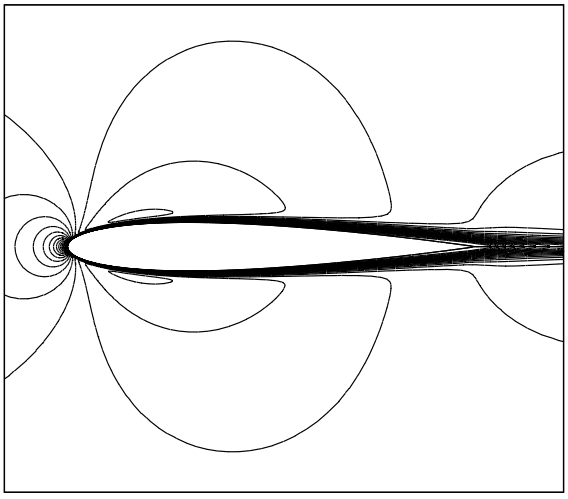

Fig. 2. Calculated Mach number contours ($M_\infty = 0.01$, $Re = 2E4$).

difference between two computational results is quite small. Therefore, this result indicates that the present method can apply not only to low speed flows but also to transonic flows.

### 5.2. Heat conduction in a solid structure

In the preconditioning approach, the fundamental equations are transformed to incompressible Navier–Stokes equations with a pseudo-compressibility term and the temperature equation when local velocities are very low. As a critical case, the present method can be further applied to the calculation of a static field by

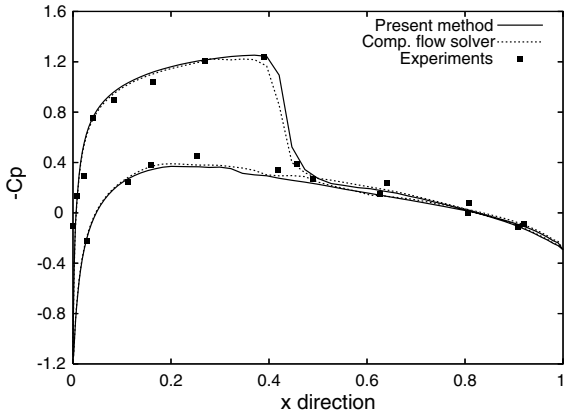


Fig. 3. Calculated pressure coefficient distributions on airfoil surface.

setting zero velocities in the field. Eq. (8) is reduced to the same equation with the equation of heat conduction when all the velocities set to zero and no pressure difference in the flow field. The equation of heat conduction in Cartesian coordinates $(x, y)$ is defined by $\partial T/\partial t = \kappa(\partial^2 T/\partial x^2 + \partial^2 T/\partial y^2)$. This equation may be commonly solved by using the relaxation method based on the SOR method and the Crank–Nicolson method.

Here, the heat conduction in a rectangular field is calculated by the present method and the calculated temperature is compared with that calculated by the equation of heat conduction using the relaxation method. A rectangular grid which has $101 \times 101$ grid points is used for both cases. The top face of the rectangular field is heated to 373 K and the other faces are fixed at 273 K. Figs. 4(a) and (b) show the calculated results obtained by the present method and by the relaxation method. Both results are quite in good

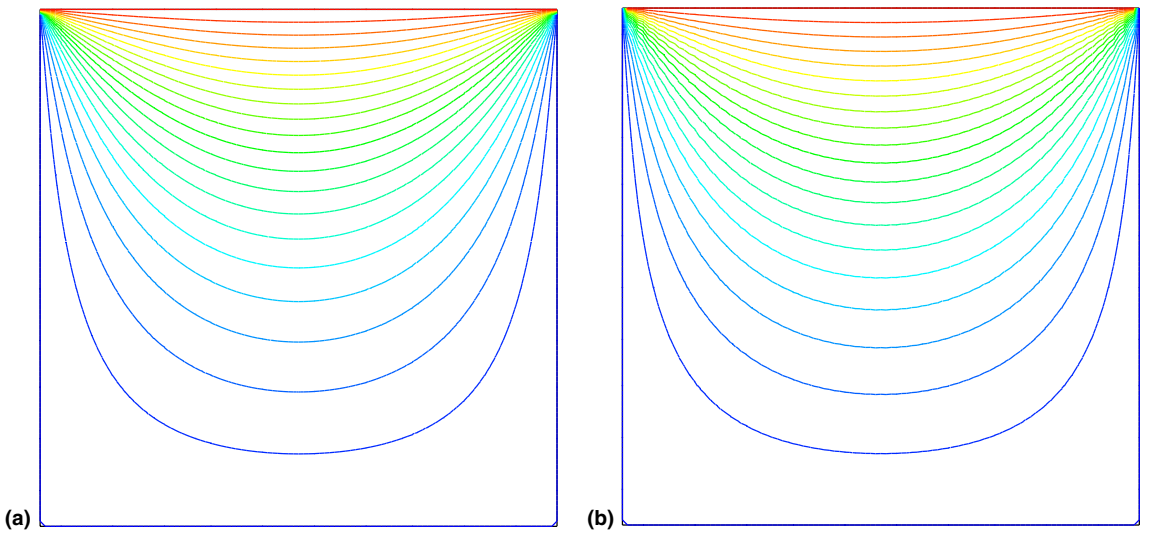


Fig. 4. (a) Calculated temperature contours (the equation of heat conduction). (b) Calculated temperature contours (the present method).

agreement with each other. This result indicates that the present method can be applied to heat conductive problems in a solid structure.

### 5.3. Transonic and low speed flows around NACA0012 airfoil with a solid structure

Transonic flows and low speed flows around NACA0012 airfoil with the heat conduction in the solid structure of the airfoil are calculated. The grid system used has $221 \times 93$ grid points around the airfoil which is the same with the previous case and $125 \times 25$ grid points in the solid structure of the airfoil. Fig. 5 shows a part of the computational grid focused on the leading edge of the airfoil. The flow conditions are specified: the angle of attack is 2°, the uniform temperature is 253.15 K, and the inner surface of the solid structure of the airfoil is heated to 293.15 K. The heat conductivity coefficient $\kappa_s$ in the solid structure is assumed as $\kappa_s = 100\kappa_a$, where $\kappa_a$ is the heat conductivity coefficient for air. The uniform Mach number is 0.75 in the transonic case and 0.01 in the low speed case.

Figs. 6(a) and (b) show the calculated temperature contours and the focused figure on the leading edge in the transonic case. The flow conditions in this case is the typical well-known conditions corresponding to the case shown in Fig. 3. A normal shock is captured upon the upper surface of the airfoil. In Fig. 6(b), temperature contours are found also in the solid structure of the airfoil. The temperature in the solid region is gradually changed from the inner surface of the solid structure to the outer surface of the airfoil.

Figs. 7(a) and (b) show the calculated temperature contours and the focused figure on the leading edge in the low speed case. The temperature distributions in the flow field are only observed in the boundary layer around the airfoil. The temperature is changed also in the solid structure as shown in Fig. 6(b). The solid region, especially that near the leading edge is more cooled in this case than that in the transonic case, because of the temperature difference at the stagnation point on the airfoil.

### 5.4. Condensate transonic flows of moist air in Laval nozzle with a solid structure

Transonic flows in a two-dimensional Laval nozzle with a solid structure are next calculated considering homogeneous nucleation and nonequilibrium condensation. The calculated pressure distributions are compared with the corresponding experiments [19]. As flow conditions, the inlet stagnation pressure is

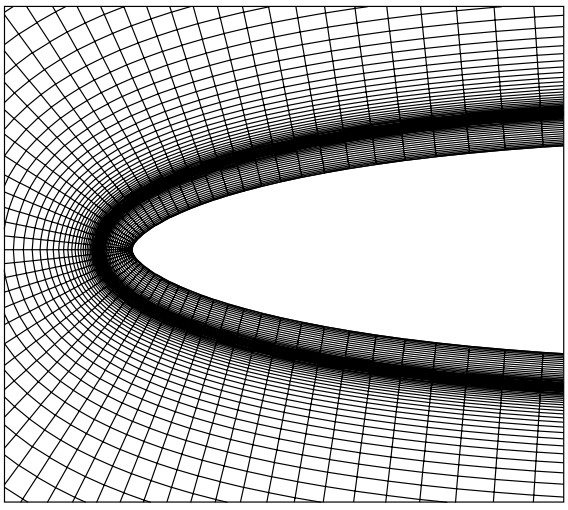

Fig. 5. A part of computational grid system.

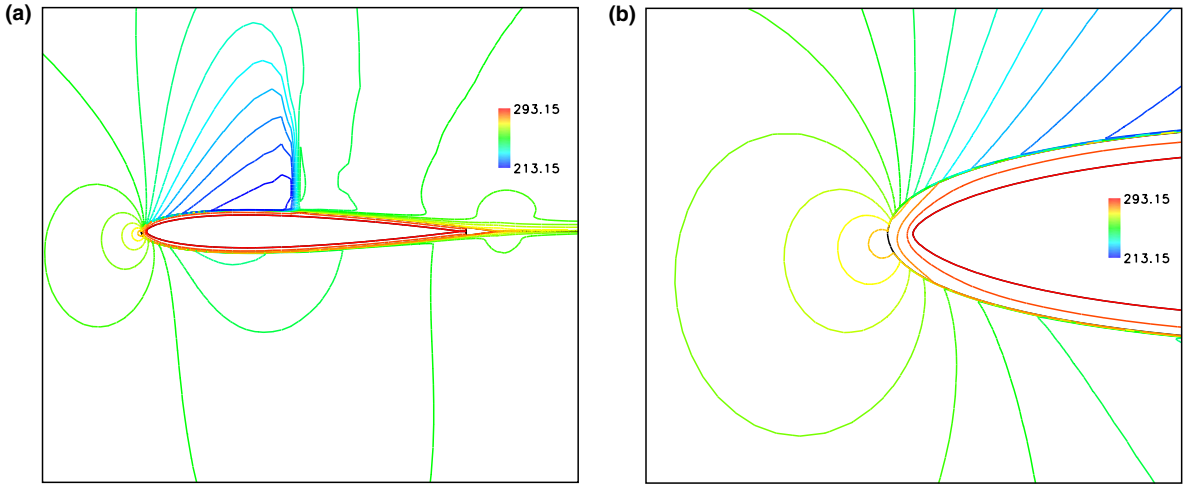


Fig. 6. (a) Calculated temperature contours. (b) Calculated temperature contours (focused on the leading edge).

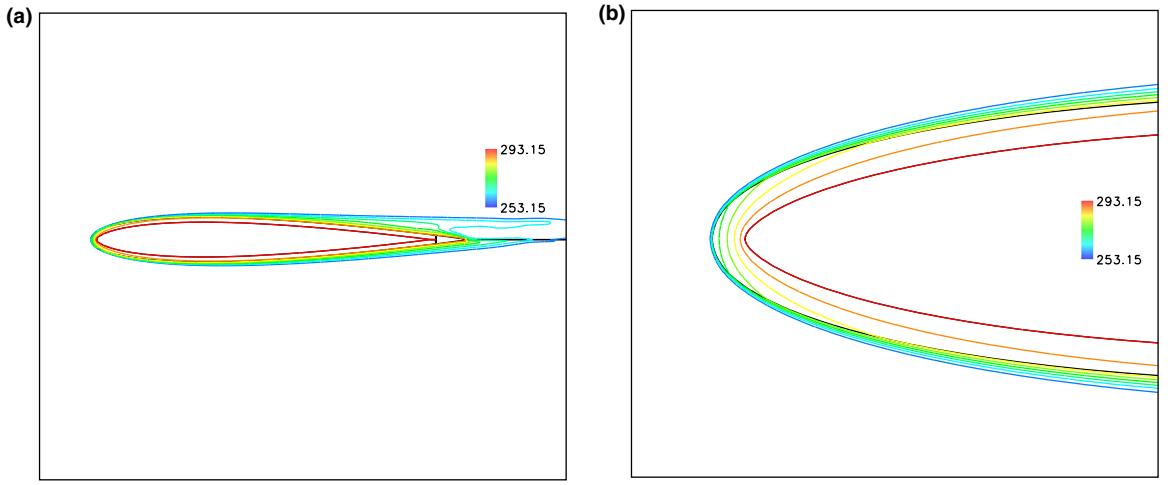


Fig. 7. (a) Calculated temperature contours. (b) Calculated temperature contours (focused on the leading edge).

$1.0 \times 10^5$[Pa], the inlet stagnation temperature is 296.6 K. Two cases of the stagnation relative humidity at 36.4% or 0% (dry air) are taken into account.

Fig. 8 shows the computational grid system. A symmetrical grid which has $151 \times 26$ grid points is used for the nozzle channel. $151 \times 21$ grid points are generated in the solid structure upon the nozzle channel. The temperature at the outer surface of the solid structure is fixed at 293.15 K. The heat conductivity coefficient $\kappa_s$ in the solid structure is assumed as $\kappa_s = 100\ \kappa_a$, where $\kappa_a$ is the heat conductivity coefficient for air.

Figs. 9(a) and (b) show the calculated temperature contours in the nozzle channel and in the solid structure for the case of the dry air and the moist air, respectively. The temperature decreases through the nozzle channel to the outlet in both cases. A difference of the temperature distributions is observed after the nozzle throat. The temperature in the case of the moist air increases after this point due to the release of latent heat when condensation occurs.

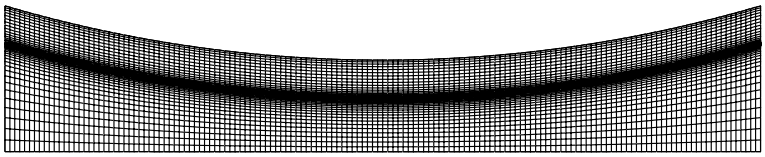

Fig. 8. Computational grid.

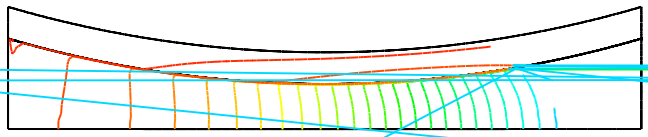

Fig. 10 shows the calculated condensate mass fraction contours for the case of the moist air. Condensed water liquid is found after the point of the onset of condensation as shown in Fig. 10. On the other hand, temperature distributions are observed in the solid region as shown in Fig. 9(a) and (b). The temperature difference between that on the outer surface of the solid structure and that on the inner surface is quite small. But, the temperature distributions in the case of the moist air are obviously influenced by the heat release due to condensation in the nozzle channel.

Fig. 11 shows the calculated pressure coefficient distributions along the symmetric line in the nozzle. The calculated result in the case of the moist air is compared with the experiments and those without condensation. Also the same case of the moist air except for the temperature fixed at 293.15 K in the solid structure is additionally calculated and the calculated result is added in Fig. 11. The present calculated distributions in the case of the moist air are in good agreement with the experiments. The effect of the heat conduction in the solid structure was trivial.

### *5.5. Natural convections with condensation around a horizontal pipe with a solid structure*

Natural convections around a horizontal pipe in atmospheric conditions are calculated as the last coupling problem. The solid structure in the pipe is also taken into account. Fig. 12 shows the computational grid system. $181 \times 45$ grid points are generated around the pipe and $181 \times 31$ grid points are generated in the pipe. The pipe has an inner flow channel occupying a water liquid at constant temperature. As flow conditions for the first case, the uniform temperature far from the pipe is 293 K, and the temperature

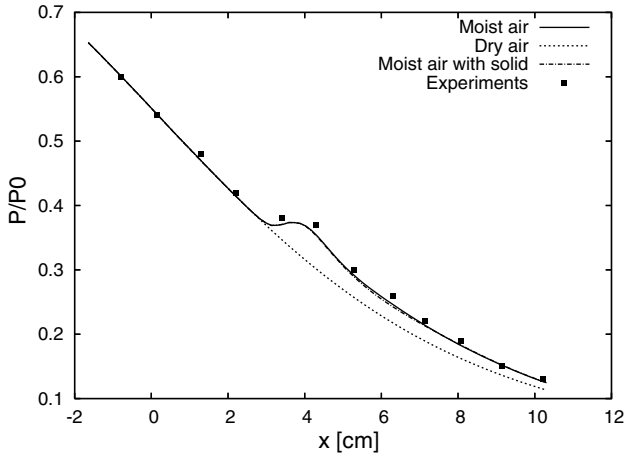


Fig. 11. Calculated pressure distributions.

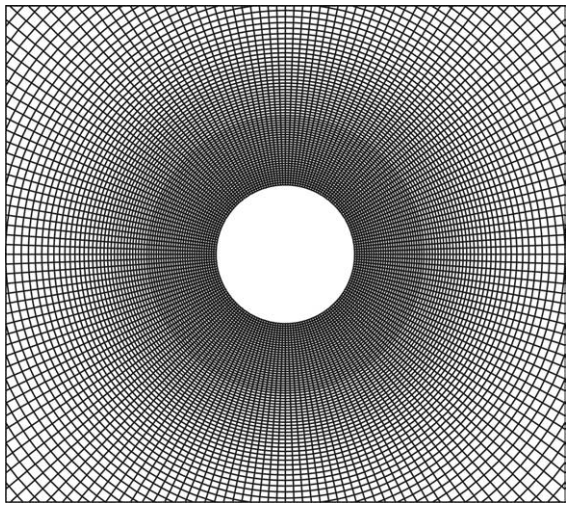

Fig. 12. Computational grid.

on the inner side of the pipe is fixed at 325.5 K assuming that the pipe channel is filled with warm water. The working gas in atmosphere is dry air. The gravitational force is added in the source term for the momentum and the energy equations. The Rayleigh number is fixed at $Ra = 10^5$. The heat conductivity coefficient $\kappa_s$ in the solid structure of the pipe is changed as $\kappa_s = \kappa_a$, $5\kappa_a$, $25\kappa_a$, $100\kappa_a$, and also the case assuming that the temperature of the solid structure is fixed at 325.5 K which is corresponding to the experiments conducted by Kuehn and Goldstein [20] is added.

Fig. 13(a) shows the calculated temperature contours around the pipe when the temperature in the solid structure of the pipe is fixed. Fig. 13(b) shows the calculated temperature contours around the pipe and in the solid structure of the pipe in the case of $\kappa_s = 25\kappa_a$. As compared with each figure, the temperature contours around the pipe are almost the same. Additionally, the solid structure of the pipe in Fig. 13(b) has temperature contours due to the heat conduction in it. Fig. 14 shows the calculated non-dimensional

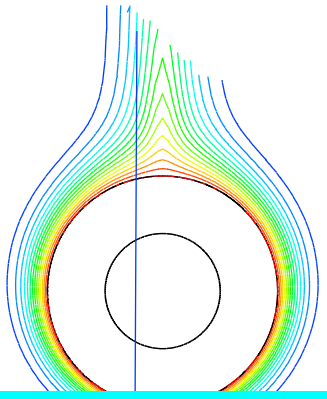

e pipe inner surface at $\theta_a = 90°$, where $\theta_a$ is the angle
the temperature ratio defined by $(T - T_\infty)/(T_w - T_\infty)$,
pipe surface and $T_w$ is the temperature at the pipe sur-
d by $Ra^{1/4}\,Y/D$ , where $D$ is the diameter of the pipe. The
pipe fixed at constant temperature is compared with the
tion could evaluate the temperature distributions quite
reases as decreasing of the heat conductivity in the solid
ctivity results in higher heat conduction in the solid

and occasionally condensation due to the phase change
next calculation, the inner surface of the pipe is cooled
) show the calculated temperature contours around the

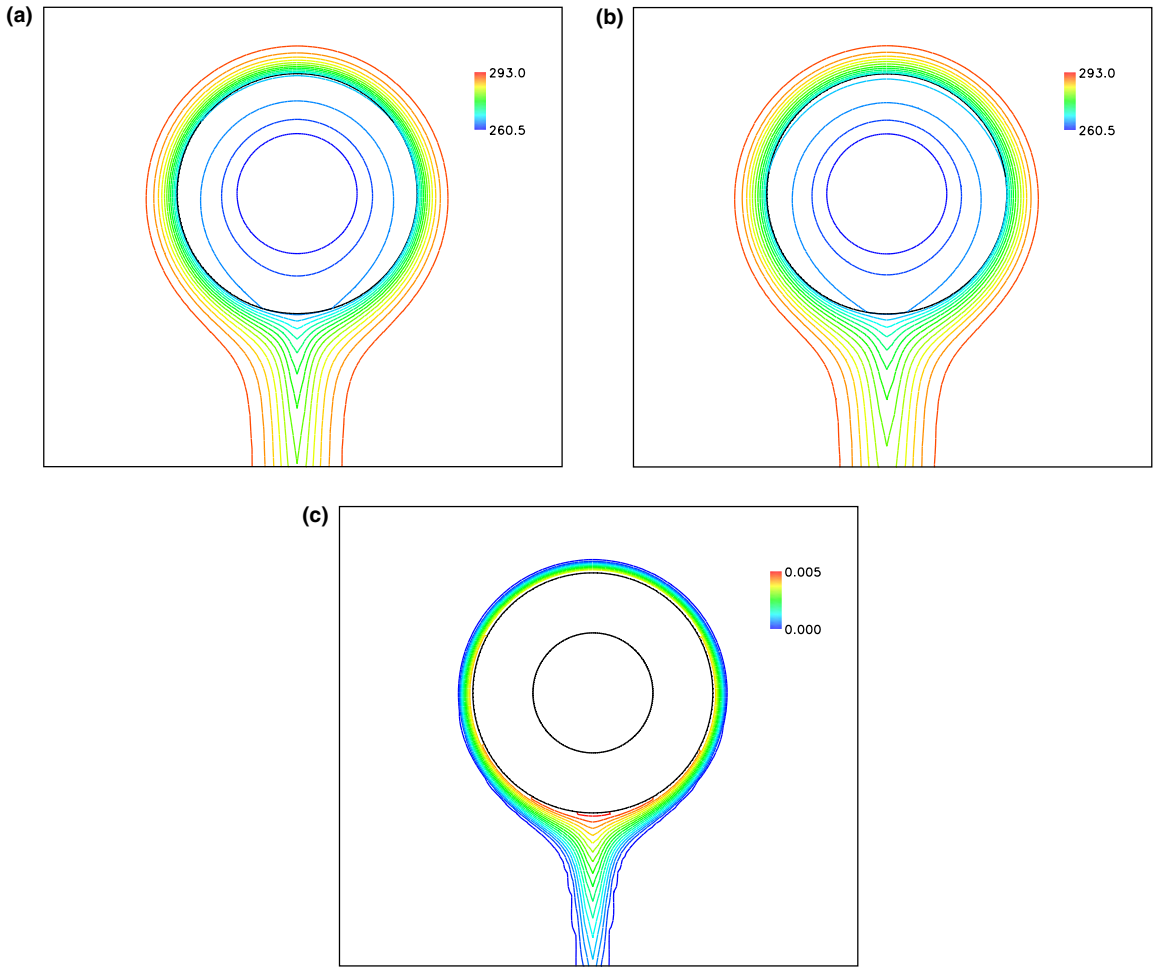


Fig. 15. (a) Calculated temperature contours (dry air). (b) Calculated temperature contours (50% humidity). (c) Calculated condensate mass fraction contours.

pipe and in the solid structure assuming a dry air and a moist air at 50% relative humidity. The cooled air around the pipe moves downward due to the negative buoyancy effect in both cases. It is found as compared with each figure that the temperature contours are slightly different. This reason can be expressed by the release of latent heat due to the condensation around the pipe. Fig. 16 shows the calculated condensate mass fraction contours in the case of the moist air. A weak condensation occurs around the pipe and the water liquid falls downward as forming a thin film over the pipe. Since this condensation releases the latent heat around the pipe, the surrounding air around the pipe is slightly heated. This heating further heats the pipe itself and results in the difference of the temperature contours between those in Fig. 15(a) and (b).

The case of 99% relative humidity is additionally calculated and the temperature distributions around the pipe are compared with those assuming the dry air and the 50% relative humidity in Fig. 16. The lower side of the pipe is relatively cooled compared with the upper side in all cases, because colder air cooled around the pipe moves downward due to the negative buoyancy effect. The latent heat released by

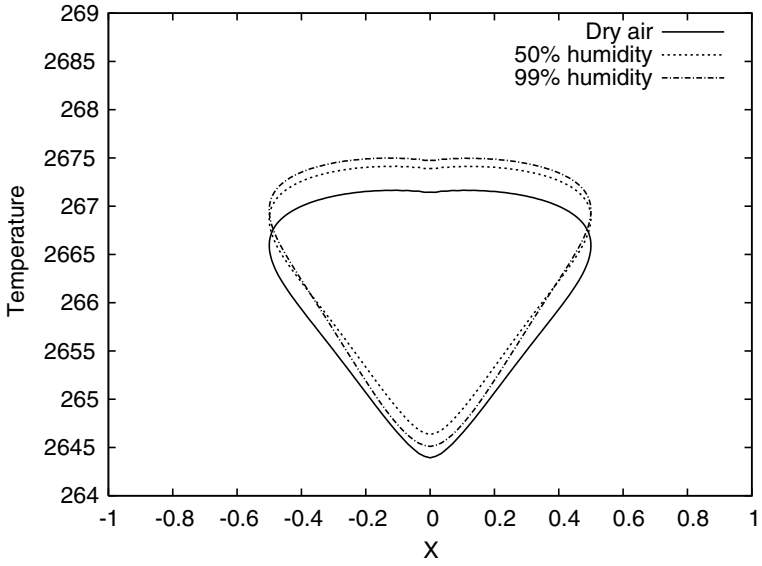


Fig. 16. Calculated temperature distributions.

condensation in the cases of the moist air slightly heats the pipe. The temperature on the upper surface of the pipe in the case of 99% relative humidity is more increased than that in the case of 50% relative humidity. On the other hand, the temperature on the lower side is rather decreased in the case of 99% relative humidity compared with that in the case of 50% relative humidity. This reason may be expressed by the increase of the condensate mass fraction in the case of 99% relative humidity. The larger mass of condensed water may accelerate the speed of convection around the pipe. The increase of the speed promotes the heat transfer in the convection. Therefore, the temperature on the lower side of the pipe in the case of 99% relative humidity is relatively decreased than that in the case of 50% relative humidity.

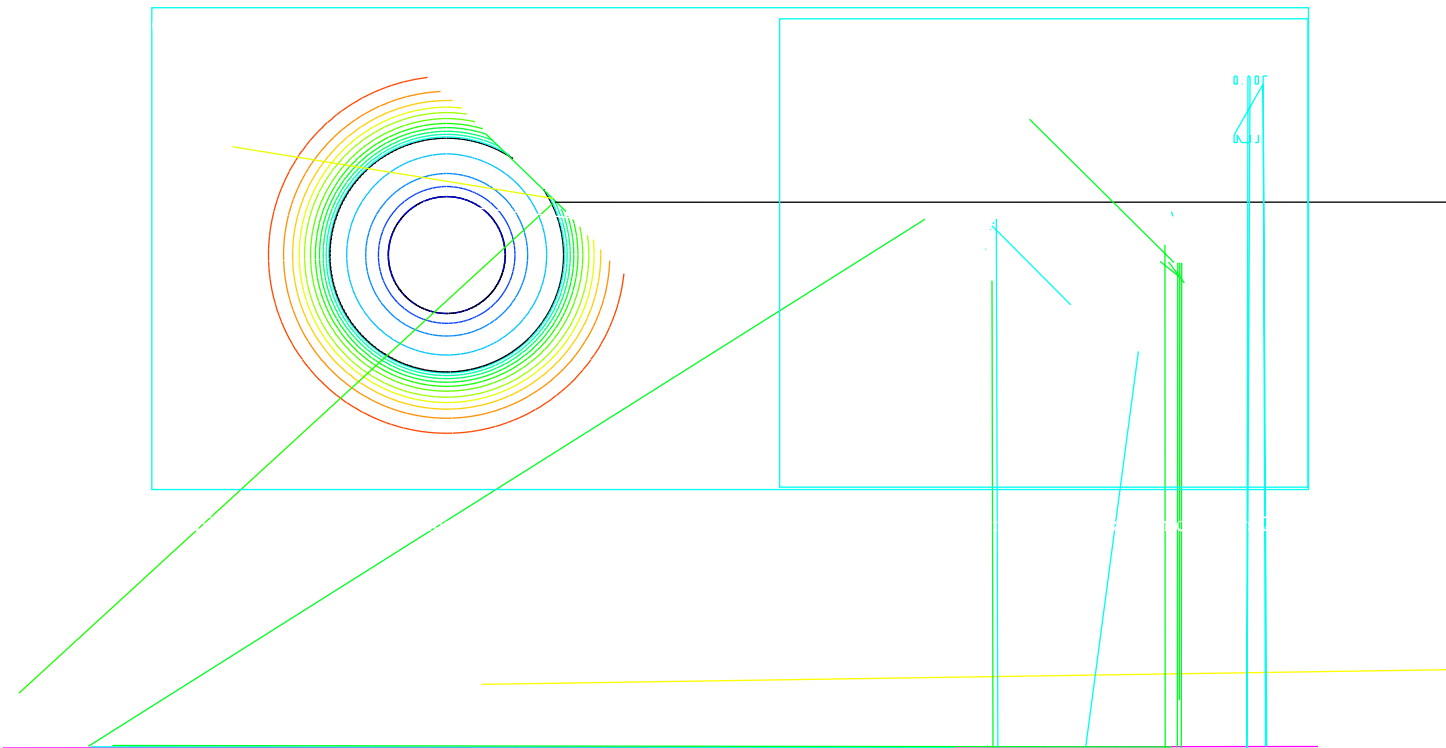

One of the most critical cases in this coupling problem is lastly calculated. We set the gravitational force to zero in the case of the 50% humidity. This may demonstrate that condensation of moist air in zero-gravity and the heat conduction in the pipe. Fig. 17(a) shows the calculated temperature contours around the pipe and in the solid structure. As compared with those results in Fig. 15(b) assuming 1g gravity, no thermal plume appears in Fig. 17(a). Only the close field around the pipe is cooled by the cooled pipe. Temperature distributions due to heat conduction are also found in the pipe. Fig. 17(b) shows the calculated condensate mass fraction contours around the pipe. The water phase is stationarily covered around the pipe. The wet region normal to the wall except for the plume region is wider than that found in Fig. 15(c). The maximum Mach number around the pipe was about $3.0 \times 10^{-7}$.

## 6. Conclusions

A numerical method for solving condensate fluid and solid coupling problems based on the preconditioning method and the condensate flow solver was presented. Heat conduction in a solid structure could be solved simultaneously by using the same method for solving condensate flows. As shown in three coupling problems such as the cases of the NACA0012 airfoil, the condensate transonic nozzle, and the heat convection around the pipe, the temperature distributions in the solid were certainly influenced by the heat transfer from the flow region. Especially, the release of latent heat due to condensation also influences the temperature distributions in the solid. One of the final targets of this study is to calculate crystal-growth problems in micro-gravity. Although the modeling of the state of crystal liquids and the coagulations still remain, the last calculated results suggest that our method can be applied to such two-phase problems with phase transition including the transitional region without any stiffness and singularities. This application is a future work of our study.

## Acknowledgement

The authors wish to acknowledge that this study was carried out as a part of the Ground-based Research Announcement for Space Utilization promoted by the Japan Space Forum.

## Appendix

$$\hat{A}_i = \begin{bmatrix} \rho_p U_i & \frac{\partial \xi_i}{\partial x_1}\rho & \frac{\partial \xi_i}{\partial x_2}\rho & \rho_T U_i & 0 & 0 & 0 \\ \frac{\partial \xi_i}{\partial x_1} + \rho_p u_1 U_i & \frac{\partial \xi_i}{\partial x_1}\rho u_1 + \rho U_i & \frac{\partial \xi_i}{\partial x_2}\rho u_1 & \rho_T u_1 U_i & 0 & 0 & 0 \\ \frac{\partial \xi_i}{\partial x_2} + \rho_p u_2 U_i & \frac{\partial \xi_i}{\partial x_1}\rho u_2 & \frac{\partial \xi_i}{\partial x_2}\rho u_2 + \rho U_i & \rho_T u_2 U_i & 0 & 0 & 0 \\ \rho_p H U_i & \rho u_1 U_i + \frac{\partial \xi_i}{\partial x_1}\rho H & \rho u_2 U_i + \frac{\partial \xi_i}{\partial x_2}\rho H & \rho_T H U_i + \rho C_p U_i & 0 & 0 & 0 \\ \rho_p(\rho_v/\rho) U_i & \frac{\partial \xi_i}{\partial x_1}\rho_v & \frac{\partial \xi_i}{\partial x_2}\rho_v & \rho_T(\rho_v/\rho) U_i & \rho U_i & 0 & 0 \\ \rho_p \beta U_i & \frac{\partial \xi_i}{\partial x_1}\rho\beta & \frac{\partial \xi_i}{\partial x_2}\rho\beta & \rho_T \beta U_i & 0 & \rho U_i & 0 \\ \rho_p n U_i & \frac{\partial \xi_i}{\partial x_1}\rho n & \frac{\partial \xi_i}{\partial x_2}\rho n & \rho_T n U_i & 0 & 0 & \rho U_i \end{bmatrix},$$

$$\Gamma^{-1} = \begin{bmatrix} \frac{\rho C_p+\rho_T C_p T-\rho_T\phi}{\rho C_p\theta+\rho_T} & \frac{u_1\rho_T}{\rho C_p\theta+\rho_T} & \frac{u_2\rho_T}{\rho C_p\theta+\rho_T} & \frac{-\rho_T}{\rho C_p\theta+\rho_T} & 0 & 0 & 0 \\ -u_1/\rho & 1/\rho & 0 & 0 & 0 & 0 & 0 \\ -u_2/\rho & 0 & 1/\rho & 0 & 0 & 0 & 0 \\ \frac{1+\phi\theta-C_pT\theta}{\rho C_p\theta+\rho_T} & \frac{-u_1\theta}{\rho C_p\theta+\rho_T} & \frac{-u_2\theta}{\rho C_p\theta+\rho_T} & \frac{\theta}{\rho C_p\theta+\rho_T} & 0 & 0 & 0 \\ -(\rho_v/\rho)/\rho & 0 & 0 & 0 & 1/\rho & 0 & 0 \\ -\beta/\rho & 0 & 0 & 0 & 0 & 1/\rho & 0 \\ -n/\rho & 0 & 0 & 0 & 0 & 0 & 1/\rho \end{bmatrix},$$

$$\Gamma^{-1}\hat{A}_i = \begin{bmatrix} \frac{(\rho C_p\rho_p+\rho_T)U_i}{\rho C_p\theta+\rho_T} & \frac{(\partial\xi_i/\partial x_1)\rho^2 C_p}{\rho C_p\theta+\rho_T} & \frac{(\partial\xi_i/\partial x_2)\rho^2 C_p}{\rho C_p\theta+\rho_T} & 0 & 0 & 0 & 0 \\ \frac{1}{\rho}\frac{\partial\xi_i}{\partial x_1} & U_i & 0 & 0 & 0 & 0 & 0 \\ \frac{1}{\rho}\frac{\partial\xi_i}{\partial x_2} & 0 & U_i & 0 & 0 & 0 & 0 \\ \frac{(\rho_p-\theta)U_i}{\rho C_p\theta+\rho_T} & \frac{(\partial\xi_i/\partial x_1)\rho}{\rho C_p\theta+\rho_T} & \frac{(\partial\xi_i/\partial x_2)\rho}{\rho C_p\theta+\rho_T} & U_i & 0 & 0 & 0 \\ 0 & 0 & 0 & 0 & U_i & 0 & 0 \\ 0 & 0 & 0 & 0 & 0 & U_i & 0 \\ 0 & 0 & 0 & 0 & 0 & 0 & U_i \end{bmatrix},$$

$$\Gamma^{-1}\hat{A}_i = L_i^{-1}\Lambda_i L_i,$$

$$L_1 = \begin{bmatrix} 1 & 0 & 0 & -\rho C_p & 0 & 0 & 0 \\ 1 & \frac{\partial\xi_1}{\partial x_1}\ell_1^+ & \frac{\partial\xi_1}{\partial x_2}\ell_1^+ & 0 & 0 & 0 & 0 \\ 0 & \frac{\partial\xi_1}{\partial x_2} & -\frac{\partial\xi_1}{\partial x_1} & 0 & 0 & 0 & 0 \\ 1 & \frac{\partial\xi_1}{\partial x_1}\ell_1^- & \frac{\partial\xi_1}{\partial x_2}\ell_1^- & 0 & 0 & 0 & 0 \\ 0 & 0 & 0 & 0 & 1 & 0 & 0 \\ 0 & 0 & 0 & 0 & 0 & 1 & 0 \\ 0 & 0 & 0 & 0 & 0 & 0 & 1 \end{bmatrix},$$

$$L_2 = \begin{bmatrix} 1 & 0 & 0 & -\rho C_p & 0 & 0 & 0 \\ 0 & -\frac{\partial\xi_2}{\partial x_2} & \frac{\partial\xi_2}{\partial x_1} & 0 & 0 & 0 & 0 \\ 1 & \frac{\partial\xi_1}{\partial x_1}\ell_2^+ & \frac{\partial\xi_2}{\partial x_2}\ell_2^+ & 0 & 0 & 0 & 0 \\ 1 & \frac{\partial\xi_2}{\partial x_1}\ell_2^- & \frac{\partial\xi_2}{\partial x_2}\ell_2^- & 0 & 0 & 0 & 0 \\ 0 & 0 & 0 & 0 & 1 & 0 & 0 \\ 0 & 0 & 0 & 0 & 0 & 1 & 0 \\ 0 & 0 & 0 & 0 & 0 & 0 & 1 \end{bmatrix},$$

$$\Lambda_1 = \begin{bmatrix} \hat{\lambda}_{11} & 0 & 0 & 0 & 0 & 0 & 0 \\ 0 & \hat{\lambda}_{13} & 0 & 0 & 0 & 0 & 0 \\ 0 & 0 & \hat{\lambda}_{11} & 0 & 0 & 0 & 0 \\ 0 & 0 & 0 & \hat{\lambda}_{14} & 0 & 0 & 0 \\ 0 & 0 & 0 & 0 & \hat{\lambda}_{11} & 0 & 0 \\ 0 & 0 & 0 & 0 & 0 & \hat{\lambda}_{11} & 0 \\ 0 & 0 & 0 & 0 & 0 & 0 & \hat{\lambda}_{11} \end{bmatrix},$$

$$\Lambda_2 = \begin{bmatrix} \hat{\lambda}_{21} & 0 & 0 & 0 & 0 & 0 & 0 \\ 0 & \hat{\lambda}_{21} & 0 & 0 & 0 & 0 & 0 \\ 0 & 0 & \hat{\lambda}_{23} & 0 & 0 & 0 & 0 \\ 0 & 0 & 0 & \hat{\lambda}_{24} & 0 & 0 & 0 \\ 0 & 0 & 0 & 0 & \hat{\lambda}_{21} & 0 & 0 \\ 0 & 0 & 0 & 0 & 0 & \hat{\lambda}_{21} & 0 \\ 0 & 0 & 0 & 0 & 0 & 0 & \hat{\lambda}_{21} \end{bmatrix},$$

$$L_1^{-1} = \begin{bmatrix} 0 & -\frac{\ell_1^-}{\ell_1^- - \ell_1^+} & 0 & \frac{\ell_1^+}{\ell_1^- - \ell_1^+} & 0 & 0 & 0 \\ 0 & \frac{1}{g_{11}(\ell_1^- - \ell_1^+)} \frac{\partial \xi_1}{\partial x_1} & \frac{1}{g_{11}} \frac{\partial \xi_1}{\partial x_2} & -\frac{1}{g_{11}(\ell_1^- - \ell_1^+)} \frac{\partial \xi_1}{\partial x_1} & 0 & 0 & 0 \\ 0 & \frac{1}{g_{11}(\ell_1^- - \ell_1^+)} \frac{\partial \xi_1}{\partial x_2} & -\left(1 - \frac{1}{g_{11}} \left(\frac{\partial \xi_1}{\partial x_2}\right)^2\right) \Big/ \frac{\partial \xi_1}{\partial x_1} & -\frac{1}{g_{11}(\ell_1^- - \ell_1^+)} \frac{\partial \xi_1}{\partial x_2} & 0 & 0 & 0 \\ -\frac{1}{\rho C_p} & -\frac{\ell_1^-}{\rho C_p(\ell_1^- - \ell_1^+)} & 0 & \frac{\ell_1^+}{\rho C_p(\ell_1^- - \ell_1^+)} & 0 & 0 & 0 \\ 0 & 0 & 0 & 0 & 1 & 0 & 0 \\ 0 & 0 & 0 & 0 & 0 & 1 & 0 \\ 0 & 0 & 0 & 0 & 0 & 0 & 1 \end{bmatrix},$$

$$L_2^{-1} = \begin{bmatrix} 0 & 0 & -\frac{\ell_2^-}{\ell_2^- - \ell_2^+} & \frac{\ell_2^+}{\ell_2^- - \ell_2^+} & 0 & 0 & 0 \\ 0 & -\left(1 - \frac{1}{g_{22}} \left(\frac{\partial \xi_2}{\partial x_1}\right)^2\right) \Big/ \frac{\partial \xi_2}{\partial x_2} & \frac{1}{g_{22}(\ell_2^- - \ell_2^+)} \frac{\partial \xi_2}{\partial x_1} & -\frac{1}{g_{22}(\ell_2^- - \ell_2^+)} \frac{\partial \xi_2}{\partial x_1} & 0 & 0 & 0 \\ 0 & \frac{1}{g_{22}} \frac{\partial \xi_2}{\partial x_1} & \frac{1}{g_{22}(\ell_2^- - \ell_2^+)} \frac{\partial \xi_2}{\partial x_2} & -\frac{1}{g_{22}(\ell_2^- - \ell_2^+)} \frac{\partial \xi_2}{\partial x_2} & 0 & 0 & 0 \\ -\frac{1}{\rho C_p} & 0 & -\frac{\ell_2^-}{\rho C_p(\ell_2^- - \ell_2^+)} & \frac{\ell_2^+}{\rho C_p(\ell_2^- - \ell_2^+)} & 0 & 0 & 0 \\ 0 & 0 & 0 & 0 & 1 & 0 & 0 \\ 0 & 0 & 0 & 0 & 0 & 1 & 0 \\ 0 & 0 & 0 & 0 & 0 & 0 & 1 \end{bmatrix}.$$

## References

[1] E. Turkel, Preconditioning methods for solving the incompressible and low speed compressible equations, J. Comp. Phys. 72 (1987) 277–298.

[2] Y.-H. Choi, C.L. Merkle, The application of preconditioning in viscous flows, J. Comp. Phys. 105 (1993) 207–223.

[3] J.M. Weiss, W.A. Smith, Preconditioning applied to variable and constant density flows, AIAA J. 33 (1995) 2050–2056.
[4] L.D. Dailey, R.H. Pletcher, Evaluation of multigrid acceleration for preconditioning time-accurate Navier–Stokes algorithems, Computers Fluid. 25 (1996) 791–811.
[5] J.R. Edwards, M.S. Liou, Low-diffusion flux-splitting methods for flows at all speeds, AIAA J. 36 (1998) 1610–1617.
[6] E. Turkel, Preconditioning techniques in computational fluid dynamics, Annu. Rev. Fluid Mech. 31 (1999) 385–416.
[7] S. Yamamoto, B.-R. Shin, Preconditioned implicit flux-splitting scheme for condensate flows, Proceedings of the Second International Conference on Computational Fluid Dynamics, Computational Fluid Dynamics 2002, Springer, 2002, pp. 112–117.
[8] P.L. Roe, Approximate Riemann solver, parameter vector and difference schemes, J. Comp. Phys. 43 (1981) 357–372.
[9] S. Yoon, A. Jameson, Lower-upper symmetric-Gauss–Seidel method for the Euler and Navier–Stokes equations, AIAA J. 26 (1988) 1025–1026.
[10] S. Yamamoto, H. Hagari, M. Murayama, Numerical simulation of condensation around the 3-D wing, Trans. JSASS 42 (2000) 182–189.
[11] S. Yamamoto, Onset of condensation in vortical flow over sharp-edged delta wing, AIAA J. 41 (2003) 1832–1835.
[12] K. Ishizaka, T. Ikohagi, H. Daiguji, A high-resolution numerical method for transonic non-equilibrium condensation flows through a steam turbine cascade, in: Proceedings of the 6th International Symposium on Computational Fluid Dynamics, vol. 1, 1995, pp. 479–484.
[13] B.S. Baldwin and H. Lomax, Thin Layer Approximation and Algebraic Model for Separated Turbulent Flows, AIAA Paper 78-275, 1978.
[14] R.M. Hall, Onset of condensation effects with an NACA 0012-64 airfoil tested in the Langley 0.3-meter transonic cryogenic wind tunnel technology, NASA TP 1385 (1979).
[15] J. Frenkel, Kinetic Theory of Liquids, Dover, New York, 1955.
[16] G.H. Schnerr, U. Dohrmann, Transonic flow around airfoils with relaxation and energy supply by homogeneous condensation, AIAA J. 28 (1990) 1187–1193.
[17] S. Yamamoto, H. Daiguji, Higher-order-accurate upwind schemes for solving the compressible Euler and Navier–Stokes equations, Computers Fluid. 22 (1993) 259–270.
[18] X. Yuan, S. Yamamoto and H. Daiguji, A Higher-resolution Shock-capturing Scheme for Simulating Unsteady Three-dimensional Transonic Flows in Turbomachinery, AIAA Paper 94-3199, 1994.
[19] C.F. Delale, G.H. Schnerr, J. Zierep, Asymptotic solution of transonic nozzle flows with homogeneous condensation.1.Subcritical flows, Phys. Fluid. A 5 (1993) 2969–2981.
[20] T.H. Kuehn, R.J. Goldstein, Numerical solution to the Navier–Stokes equations for laminar natural convection about a horizontal isothermal circular cylinder, Int. J. Heat Mass Transfer 23 (1980) 971–979.